Extreme Mechanics Letters 45 (2021) 101281

Contents lists available at ScienceDirect

Extreme Mechanics Letters

journal homepage: www.elsevier.com/locate/eml

Flow-coupled cohesive interface framework for simulating heterogeneous crack morphology and resolving numerical divergence in hydraulic fracture

Xin Cai [a,b], Wei Liu [a], Xinpu Shen [a], Yanfei Gao [b,*]

[a] School of Petroleum Engineering, China University of Petroleum, Qingdao 266580, China
[b] Department of Materials Science and Engineering, University of Tennessee, Knoxville, TN 37996, USA

ARTICLE INFO

Article history:
Received 12 January 2021
Received in revised form 24 February 2021
Accepted 10 March 2021
Available online 18 March 2021

Keywords:
Cohesive zone model
Hydromechanical coupling
Fracking morphology

ABSTRACT

A user-friendly and generic finite element framework for simulating hydraulic fracture with a complex crack network in unconventional oil and gas exploitation is developed in this work with the following unique features. While the cohesive zone model (CZM) removes crack singularities, its finite element simulations suffer numerical convergence problem during crack nucleation and growth, which can be regularized by a fictitious viscosity approach. The decoupling of cohesive-cracked solid and fluid into separate free body diagrams allows the development of a weak-form finite element formulation for the former and a finite-difference approach for the transport analysis in the latter. Enforcing the Kirchhoff condition in polycrystalline geomaterials allows the study of the fluid-driven complex fracture propagation process. Our method has been verified by analytical solutions, and then employed to simulate the synergistic roles of confining pressure and grain boundary anisotropy on the fracking morphology. Numerical implementation into a user-defined element (UEL) subroutine in ABAQUS provides easy adaptation and further development for the research community.

1. Introduction

Hydraulic fracturing, or commonly called fracking, has been one of the primary engineering tools for improving well productivity, especially for unconventional reservoirs such as shale or tight sand reservoirs [1,2]. Upon the injection of highly pressurized fluid, cracks may nucleate and propagate in these sedimentary rocks, thus allowing the passage and harvesting of the stored natural gas. The hydromechanical coupling lies on three main physical processes: rock deformation induced by the fluid pressure acting on the weak surfaces, the fluid flow in the cracked pathways, and the crack morphology [3]. As will be explained shortly, despite tremendous technological advancements, it still remains difficult to accurately predict the geometry of hydraulic fractures deeply under the ground, which thus prevents further quantitative studies such as seismic detection and monitoring.

Due to many insurmountable difficulties in measuring the hydraulic fracture processes, a variety of numerical simulation approaches have been employed in modeling hydraulic fractures. With the help of prior analytical solutions for the stress intensity factor calculations, several analytical models, such as the PKN model [4] and KGD model [5], have been proposed to predict the shape and size of a hydraulic fracture based on simplifications regarding the planar geometry, homogeneous media, and uniform fluid pressure distribution along the fracture. These solutions are used for verification and validation of numerical models, such as the boundary element method (BEM) [6,7], discrete element method (DEM) [8–10], and finite element method (FEM) [11–13]. BEM is a very efficient method to simulate fracture propagation because only the boundary of the simulation domain is discretized, but it is restricted to homogeneous and isotropic elastic media and simple fracture morphology [14]. Since it treats the rock mass as an ensemble of individual particles, DEM has the advantage of simulating relatively complex fracture geometry, but its disadvantages lie on the time-consuming calibration process and the restriction on particle–particle interactions [15]. In the FEM community, the cohesive zone model (CZM) and the extended finite element method (XFEM) are the most widely used techniques. XFEM allows a fracture to diverse its course to a new direction, but it is rather difficult to use this approach for multi-physical and multi-fracture problems [16,17]. CZM treats the entire solid as the sum of a weak interface and two adjoining bulks, which can then be easily extended with computer-aided design to generate multiple weak interfaces for polycrystalline and granular materials [18,19]. The prescribed traction–separation law in

---

[*] Corresponding author.
E-mail addresses: b16020085@s.upc.edu.cn (X. Cai), liu.wei@upc.edu.cn (W. Liu), 20180011@upc.edu.cn (X. Shen), ygao7@utk.edu (Y. Gao).

https://doi.org/10.1016/j.eml.2021.101281
2352-4316/

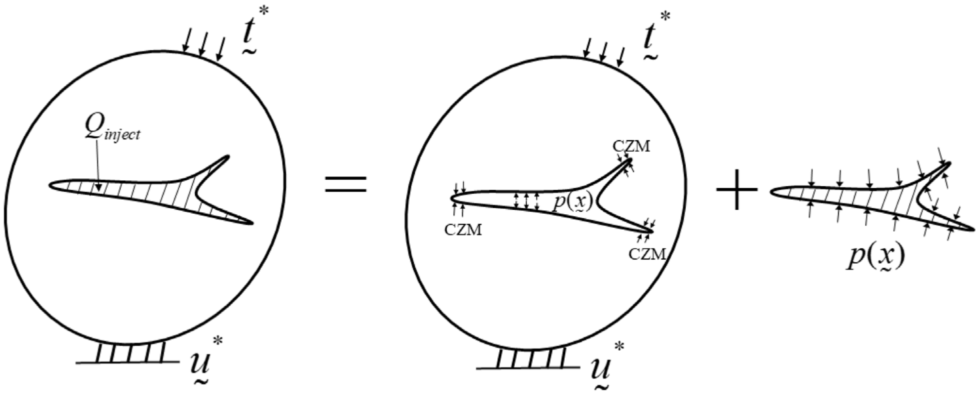

Fig. 1. The hydromechanical problem can be regarded as a sum of two free body diagrams: a cracked solid (with cohesive tractions at the tip and crack-surface pressures from fluid) and a fluid transport problem with a pressure field.

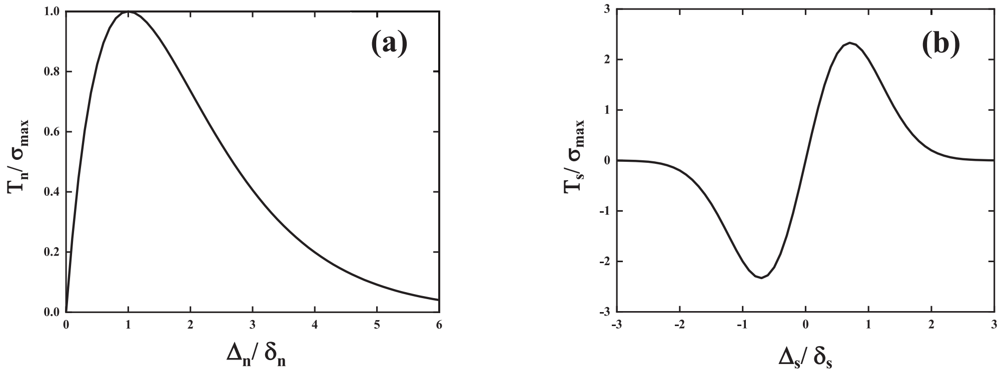

Fig. 2. Ttraction–separation relationship from the cohesive zone law [20]: (a) pure normal loading, and (b) pure tangential loading, where $q = 1$ and $r = 0$.

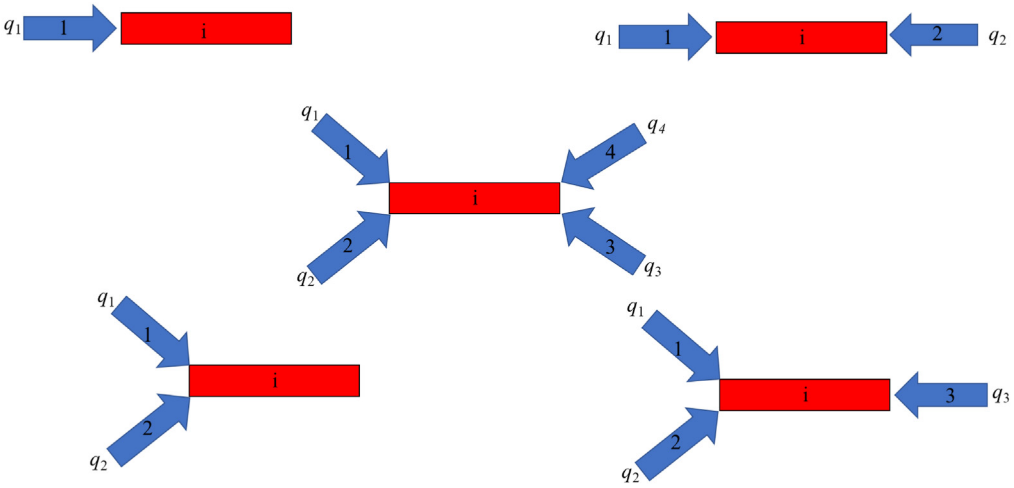

Fig. 3. Element connectivity showing various flow patterns into a given element i, whereas arrows indicate the flow directions. Eq. (9) is derived based on the balance of the mass accumulation rate inside this element and the sum of fluxes into and out of this element.

the CZM removes the crack tip singularities in the linear elastic fracture mechanics.

While CZM has been widely used in hydraulic fracturing simulations [21–25], many practical hurdles need to be resolved beyond simple benchmark studies on verification and validation. *First*, micro-seismic monitoring of hydraulic fracturing processes in unconventional reservoirs shows that hydraulic fractures may propagate as a complex fracture network with lots of branches [26]. Modeling such hydromechanically coupled processes associated with complex fracture morphology is a challenging problem, as the transport analysis needs ad hoc continuity condition even though the mere fracture analysis does not pose a challenge when cohesive interface elements are introduced along all possible pathways. *Second*, CZM studies in literature can be grouped into two categories: those which rely on existing capabilities in ABAQUS [21–24], and others with homemade codes [25,27–29]. In the former (e.g., [21–24]), it should be pointed out that ABAQUS treats nodal pressure as one of the field

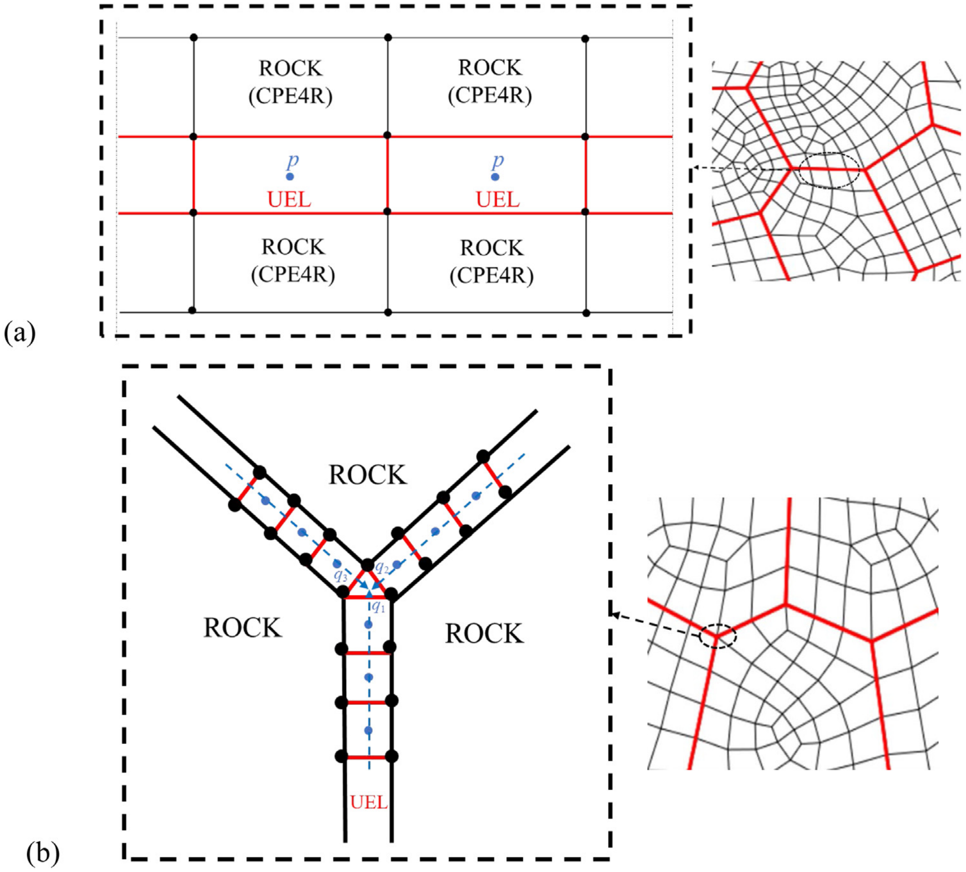

Fig. 4. Schematic illustration of the user-defined cohesive elements inserted between the surrounding grains: (a) grain boundaries, and (b) triple junctions.

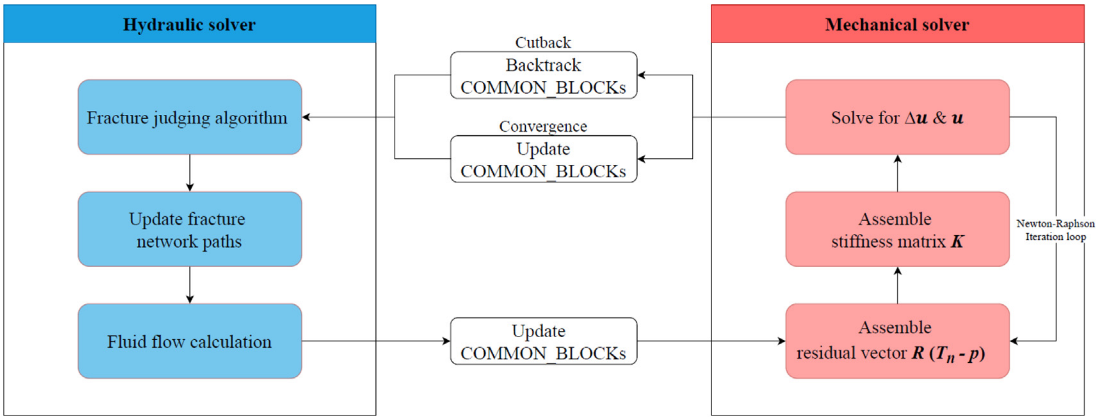

Fig. 5. Schematic illustration of the hydromechanical coupling.

parameters, which does not allow the users to introduce constitutive model other than the Newtonian viscous fluid. Meanwhile, the CZM law is restricted to a bilinear law (or initially linear followed by an exponential decay), which again does not allow important features such as hysteresis and dilatancy for geomaterials to be incorporated. Decoding the finite element formulation and yet providing a user-friendly interface will open tremendous opportunities in realistic applications, especially in taking advantage of computer-aided engineering modules in ABAQUS. Nguyen et al. [25] presented a complete formulation based on the weak forms for both fluid flow and the fracture problem, but their results are still yet to be proven in simulating complex fracture patterns. *Third*, while CZM smears out the stress singularity, it still faces numerical divergence problem when the crack bridging zone (details given later in this paper) is much smaller than the crack size. From the mechanics point of view, this is an intrinsic problem corresponding to the snap-back instability when multiple solutions are possible. A preliminary assessment by the authors show that many literature studies have chosen parameters to ensure unphysically large bridging-zone size, which certainly avoids the snap-back instability but surely casts doubts on the validity of simulation results. A simple technique for avoiding convergence problems in finite element simulations of cohesive cracks can be introduced by adding a fictitious viscosity in our previous work [30].

The objective of this study is to introduce a numerical framework for the hydromechanically coupled processes, with key features including:

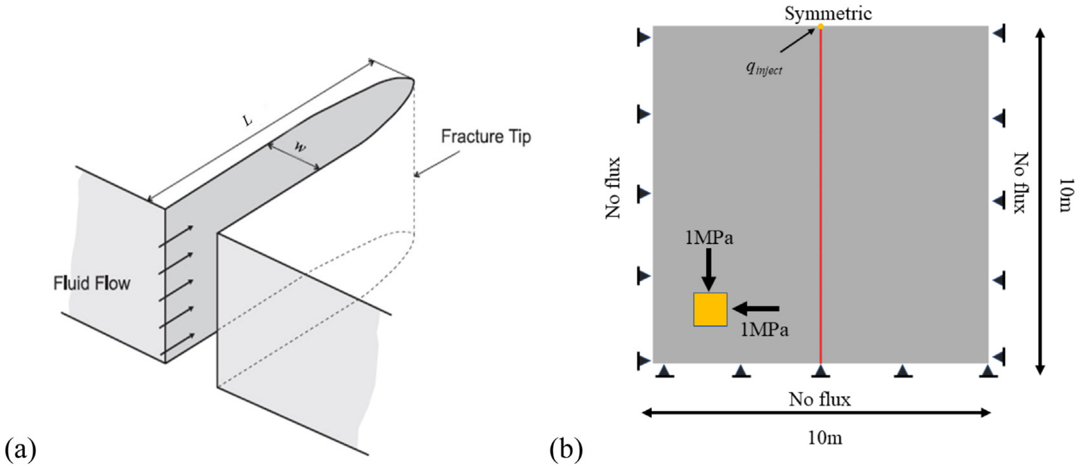

Fig. 6. (a) Geometric representation for the plane-strain KGD model. (b) Model setup and boundary conditions for the fluid-driven fracture propagation simulation.

Table 1
Parameters used for the simulation of the KGD problem.

Parameters	Values
Rock Young's modulus, E (GPa)	30
Rock Poisson's ratio, υ	0.25
Mesh size, e (m)	0.05
Maximum traction stress, σ_{max} (MPa)	3
Characteristic normal lengths, δ_n (μm)	20
Characteristic tangential lengths, δ_t (μm)	20
Normalized fictitious viscosity	0.0001
Fluid viscosity, μ (Pa s)	0.001
Fluid injection rate per thickness of reservoir, q_{inject} (m^3/(s m))	0.001
Leak-off coefficient, c_l (m^3/Pa)	0

Table 2
Mechanical and hydraulic parameters for reservoir models.

Parameters	Value
Young's modulus, E (GPa)	30
Poisson's ratio, υ	0.25
Voronoi grain size (mean), (m)	0.2
Vertical confining stress, σ_H (MPa)	7
Horizontal confining stress, σ_h (MPa)	5
Minimum of traction strength, σ_{max} (MPa)	2
Minimum of characteristic normal lengths, δ_n (μm)	150
Minimum of characteristic tangential lengths, δ_t (μm)	150
Normalized fictitious viscosity	0.0001
Fluid viscosity, μ (Pa s)	0.001
Injection rate, q (m^2/s)	0.01
Leak-off coefficient, c_l (m^2/Pa)	0

- A finite element framework for the cohesive cracks with a fictitious viscosity approach to regularize the snap-back instability;
- A finite difference method for fluid transport equation with built-in Kirchhoff conditions to ensure continuity and to address arbitrary crack morphology;
- The coupling of the above two processes is made possible via the crack surface pressure field, and iterative implicit–explicit algorithms and staggered time incrementation to ensure numerical performance;
- All the above are built into a user-defined element (UEL) subroutine in ABAQUS, suitable for easy integration with computer-aided engineering.

The numerical details for the above bullets will be given in Section 2, and the code will be validated to analytical solutions in Section 3. To demonstrate our capability of simulating complex fracture morphology, Section 4 presents a hydraulic fracturing example with various degrees of grain boundary anisotropy in fracture energy, which open room for further studies and experimental comparisons. Summary will be given in Section 5 in the end.

2. Numerical framework

As shown in Fig. 1, the crack problem and fluid transport problem are handled separately by two free body diagrams, with the connection being the crack-surface pressure field. For the cracked solid, the finite element framework is built upon the following principle of virtual work,

$$\int_{\Omega} \sigma_{ij} \delta u_{i,j} dV + \int_{cohesive} T_i \delta \Delta_i dA = \int_{all} t_i \delta u_i dA, \tag{1}$$

where σ_{ij} are the stress tensor and $u_{i,j}$ are the displacement gradients in the volume integral, T_i and Δ_i are tractions and separations of the cohesive interface in the surface integral on the left hand side, t_i are the surface tractions (including the applied traction on the external boundary and the pressure field on the cohesive surfaces) of the surface integral on the right hand side, and δ is the variational operator. Latin subscripts run from 1 to 3, and summation convention is implied over repeated indices.

For a given cohesive element, we can define a local coordinate system as spanned by the element tangent $\mathbf{s}$ and normal $\mathbf{n}$ with right hand convention. The upper and lower surfaces are $S^{\pm}$, and the displacement jumps define the CZM separation by,

$$\Delta_n = \left(\mathbf{u}^{+} - \mathbf{u}^{-}\right) \cdot \mathbf{n},\ \Delta_s = \left(\mathbf{u}^{+} - \mathbf{u}^{-}\right) \cdot \mathbf{s}. \tag{2}$$

The CZM tractions relate to the Cauchy stress in adjoining solids by

$$T_n = \mathbf{n} \cdot \boldsymbol{\sigma} \cdot \mathbf{n},\ \ T_s = \mathbf{n} \cdot \boldsymbol{\sigma} \cdot \mathbf{s}. \tag{3}$$

In local coordinates, the constitutive relationship between the traction vector (T_n, T_s) and the separation (Δ_n, Δ_s) is defined by a potential function Φ such that

$$T_n = \frac{\partial \Phi}{\partial \Delta_n},\ \ T_s = \frac{\partial \Phi}{\partial \Delta_s} \tag{4}$$

Various forms of cohesive zone models have been proposed for this potential, all of which can be easily implemented in our UEL. For an illustrative purpose, we use the Xu–Needleman version [20],

$$\Phi\left(\Delta_n, \Delta_s\right) = \Phi_n + \Phi_n \exp\left(-\frac{\Delta_n}{\delta_n}\right)\left\{\left[1 - r + \frac{\Delta_n}{\delta_n}\right]\frac{1-q}{r-1}\right.$$

$$-\left[q+\left(\frac{r-q}{r-1}\right)\frac{\Delta_n}{\delta_n}\right]\exp\left(-\frac{\Delta_s^2}{\delta_s^2}\right)\Bigg\}, \tag{5}$$

$$q=\frac{\Phi_s}{\Phi_n},\, r=\frac{\Delta_n^*}{\delta_n} \tag{6}$$

where Φ_n is the work of normal separation, Φ_t is the work of tangential separation, δ_n and δ_s are corresponding characteristic lengths, and Δ_n^* is the value of Δ_n after complete shear separation. The representative traction–separation relations resulting from Eq. (5) are given in Fig. 2, where the maximum traction is $\sigma_{\max}=\frac{\Phi_n}{\delta_n \exp(1)}$ and Φ_n can be interpreted as the fracture energy under the Mode I loading condition.

The cohesive interface simulations are often limited by the occurrence of a snap-back instability, resulting singular stiffness matrix in the Newton–Raphson iteration. Such numerical convergence problem can be solved by introducing a small viscosity to the derivatives of the cohesive constitutive Eq. (5),

$$T_n=\sigma_{\max}\frac{\Delta_n}{\delta_n}\exp\left(1-\frac{\Delta_n}{\delta_n}-\frac{\Delta_s^2}{\delta_s^2}\right)+\zeta_n\frac{d}{dt}\left(\frac{\Delta_n}{\delta_n}\right), \tag{7}$$

$$T_s=2\sigma_{\max}\left(\frac{\delta_n}{\delta_s}\right)\left(\frac{\Delta_s}{\delta_s}\right)\exp\left(1-\frac{\Delta_n}{\delta_n}-\frac{\Delta_s^2}{\delta_s^2}\right)+\zeta_t\frac{d}{dt}\left(\frac{\Delta_s}{\delta_s}\right). \tag{8}$$

where $q=1$ and $r=0$ are adopted for simplicity. The appropriate choice of viscosity parameters, ζ_n and ζ_t can be found in [30], where a detailed finite element procedure is also described. A nonlinear finite element implementation for Eq. (1) also requires the Jacobian matrix, comprised of the differentiation of (T_n, T_s) with respect to (Δ_n, Δ_s). It should be noted that the viscous terms in Eqs. (7) and (8) also contribute to the Jacobian upon the finite difference formulation of these two rate terms. Essentially, when the snap-back instability occurs, the original Jacobian becomes singular, but the added terms, proportional to $\zeta_n/\Delta t$, regularizes this singularity and forces the convergence of Newton–Raphson iteration.

We now move on to the fluid flow, as governed by the momentum and mass transport equations. Degenerating from the general Navier–Stokes equation, the former is given by the Poiseuille's law in laminar flow. Substituting this to the latter will convert the continuity equation into the classic lubrication equation [1,2], given by

$$\frac{\partial w}{\partial t}+q_l=\frac{1}{12\mu}\nabla\cdot\left(w^3\nabla p\right)+Q\left(t\right)\delta\left(\mathbf{x}-\mathbf{x}^*\right), \tag{9}$$

where p is the pressure of the fluid inside the fractures , w is the fluid channel thickness (i.e., this is the crack opening displacement, Δ_n, in Eq. (2)), μ is the viscosity of the injected fluid, q_l is the leak-off flow rate to the surrounding solids, and $Q\left(t\right)$ is the fluid injection rate at a point source of $\mathbf{x}=\mathbf{x}^*$. Since the fluid flow is confined into 1D paths, the divergence operator in Eq. (9) is equivalent to the net flux at the two end points of any cohesive element along the arc direction.

These governing equations will be solved by finite difference (FD) with mixed implicit–explicit integration scheme. Upon discretization, we note that any element is connected by at most four other elements, as shown by the topological connectivity in Fig. 3, the flux direction flowing into the element is defined as positive. Summing the fluid flow from neighboring elements to element i from the Poiseuille equation, we have

$$\sum_j q_{ji}=\frac{1}{12\mu}\sum_{j=1\sim4}\left\{\frac{\left[\left(w_i^{n+1}+w_j^{n+1}\right)/2\right]^3\left(p_j^n-p_i^{n+1}\right)}{\left(L_i+L_j\right)/2}\right\}, \tag{10}$$

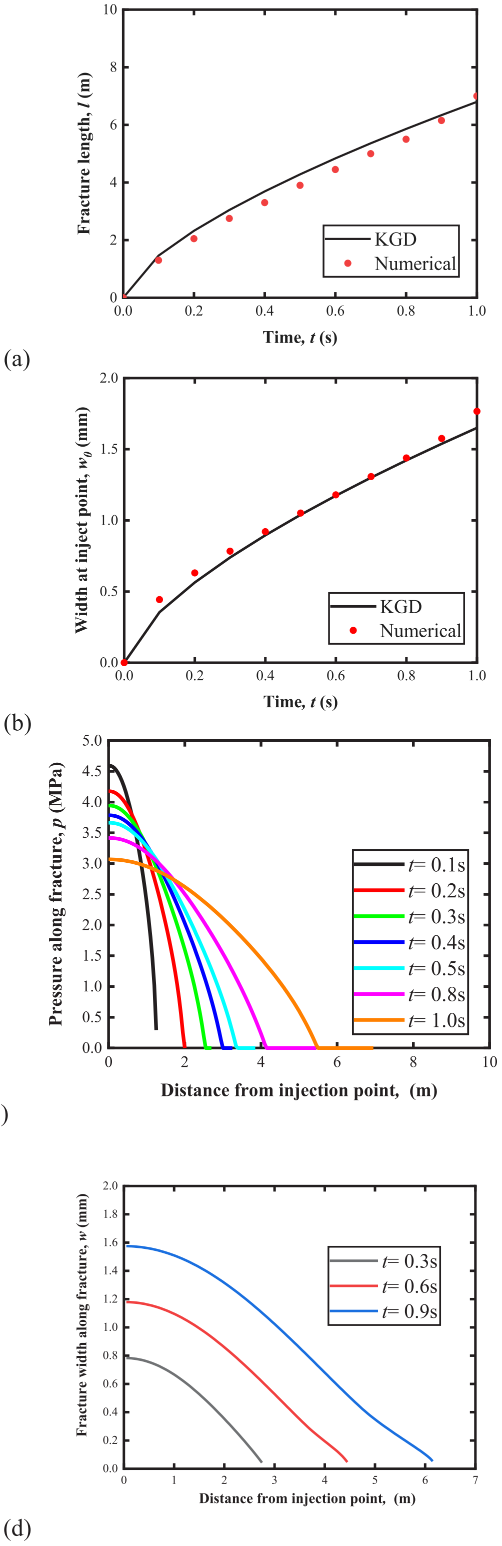

Fig. 7. Comparisons between numerical simulation and KGD solutions: (a) fracture length, (b) crack opening displacement, (c) pressure gradients along the crack path, and (d) crack opening displacements along the crack path.

where L_i is the element length, i and j are element numbers, and the superscripts n and $n+1$ denote quantities evaluated at time t_n and $t_{n+1}=t_n+\Delta t$, respectively.

The continuity equation (9) includes the injection, leak-off, and fluid flow exchange at the two end points of a given element,

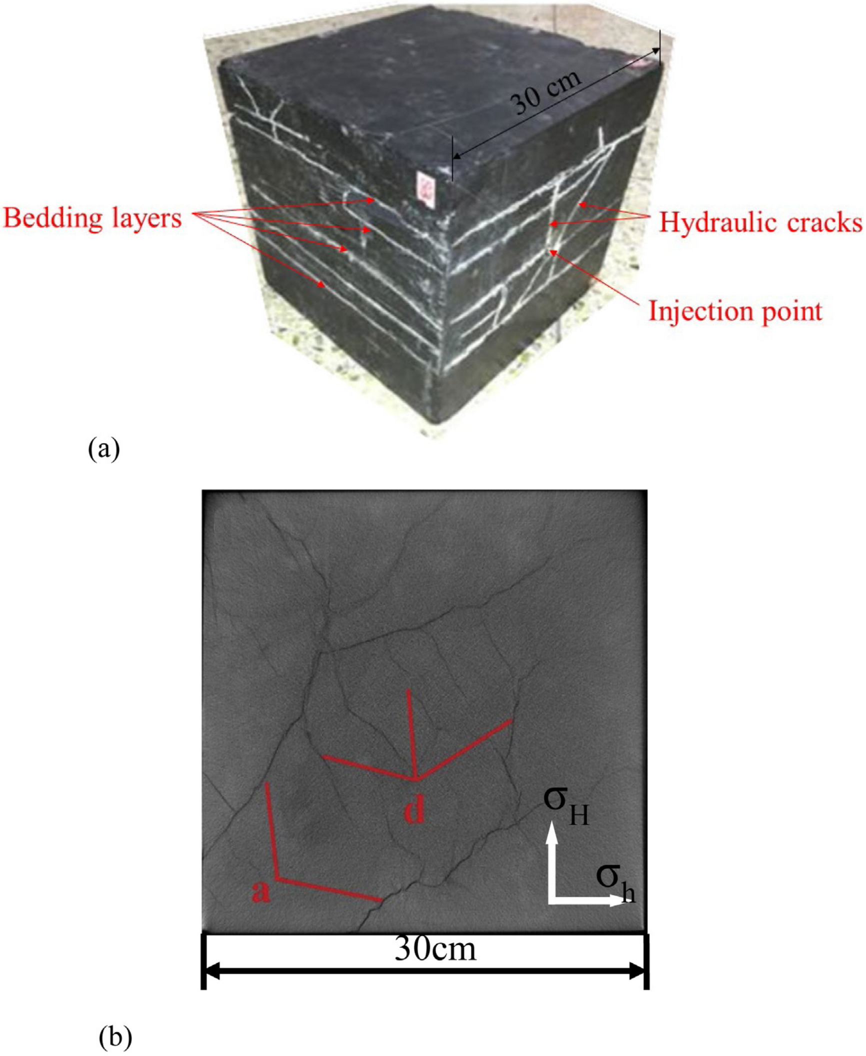

Fig. 8. (a) Outcrop of Lu Jiaping shale formation showing complex fracking patterns [31]. (b) In such anisotropic shales under hydraulic fracturing test, the fracture patterns usually consist of several main opening cracks (labeled by "a") and shear-type tributary cracks (labeled by "d") [32].

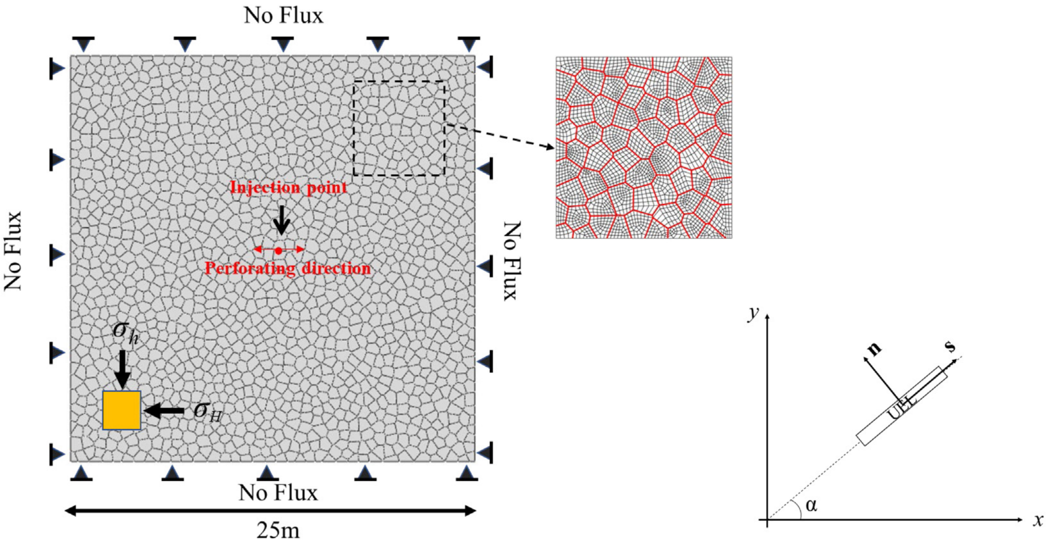

Fig. 9. Model setup for a polycrystalline rock with grain-boundary cohesive elements. The element tangent defines the orientation angle of α.

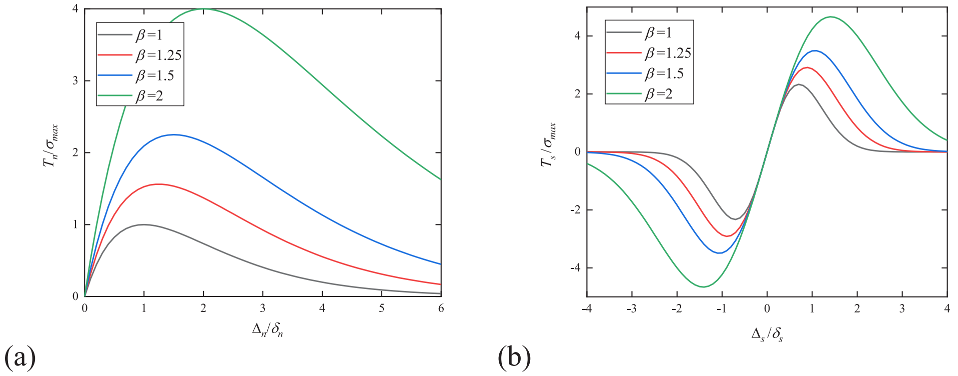

Fig. 10. The interface traction–separation relationship with respect to β: (a) normal direction (when Δ_s vanishes), and (b) tangential direction (when Δ_n vanishes).

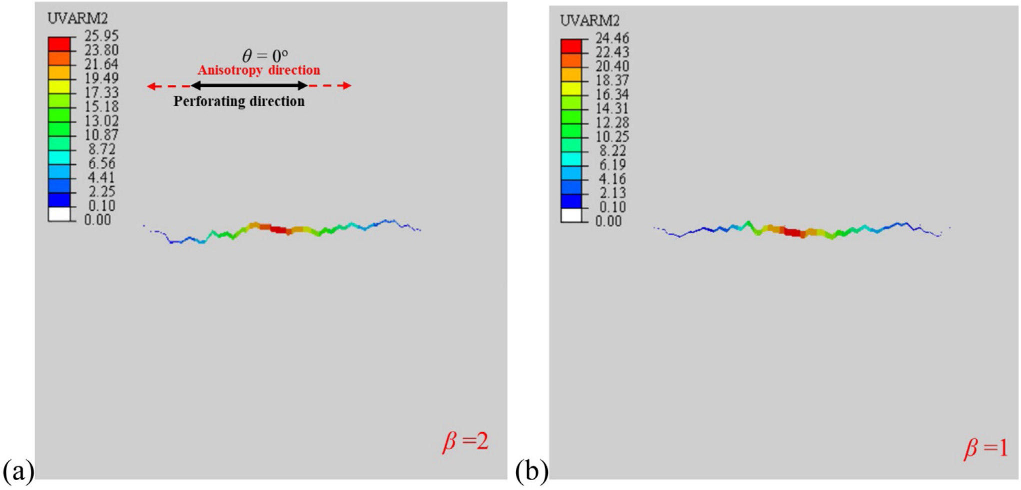

Fig. 11. Fracture morphologies due to fluid injection (Fig. 9) with material anisotropy direction lying horizontally (i.e., $\theta = 0$): (a) $\beta = 2$, and (b) $\beta = 1$.

$$\frac{w_i^{n+1}-w_i^n}{\Delta t}+c_l\left(p_i^n-p_r\right)=\frac{1}{L_i}\sum_j q_{ji}+Q\left(t^{n+1}\right)\delta\left(\mathbf{x}-\mathbf{x}^*\right), \quad (11)$$

where the leak-off flow rate takes the linear form by Darcy equation for permeable solids, with c_l being the fluid leak-off coefficient and p_r being the pore pressure in the adjacent solid. The Dirac delta term needs to be smeared out at the element receiving the fluid injection. Substituting Eq. (10) into Eq. (11) will give an increment form to solve for $\Delta p_i = p_i^{n+1} - p_i^n$. The parabolic nature of Eq. (9) puts a restriction on the time increment Δt and element length L. More specifically, we choose the time increment according to the following [33,34],

$$\Delta t=\min\left\{\Delta t^*, \min\left\{\frac{w_i L_i}{2\sum_j q_{ji}}, i=1,\ldots,N_{element}\right\}\right\}, \quad (12)$$

where $N_{element}$ is the total number of interface elements, $\sum_j q_{ji}$ is the total flow rate into element i, and Δt^* is dictated from element size by the Lax condition, $\Delta t^* \leq 12\mu L^2$ (e.g., taken as 5×10^{-5} s in our examples later in Tables 1 and 2).

In a polycrystalline material, the grain boundaries are discretized by a number of 2D four-node user-defined elements, on which the FEM procedure for the traction–separation relationship and the FD procedure for the fluid flow are conducted. As shown in Fig. 4, the initial gap is zero, $\Delta_n = \Delta_s = 0$, i.e., the top and bottom nodes collapse onto each other, although the drawing exaggerates the element thickness for the sake of illustration. Of course, pre-existing cracks or foreign objects can be easily added. The rock grains are discretized with four-node plane strain elements with reduced integration. The connectivity condition in Fig. 4(a) suggests two single-channel flows on the two end points of such a grain-boundary cohesive element, while there will be three flows into the element adjacent to the trip junction in Fig. 4(b). Kirchhoff conditions are automatically satisfied from Eq. (10) and Fig. 3.

The above FEM/FD formulation encounters two practical difficulties in the implementation into the user-defined element (UEL) subroutine in ABAQUS: (i) nonlocal information acquisition, and (ii) time incrementation. According to Eq. (10), the Poiseuille flow fluxes need to be computed with the knowledge of neighboring elements, while ABAQUS UEL does not provide a function to access such nonlocal information. This difficulty can be resolved by the COMMON BLOCK technique for data storage and acquisition. As illustrated in Fig. 5, several data tables have been created to store the information of cohesive element connectivity (for the sake of Poiseuille flow), interface-bulk element connectivity (for the sake of Darcy flow), and pressure values for all cohesive elements at t_n and t_{n+1}. In UEL, given $\mathbf{u}^n$ and $\mathbf{u}^{n+1}$, together with p_i^n table in the COMMON BLOCK, the pressure values will be updated to p_i^{n+1} from Eqs. (10) and (11), and then stored in the COMMON BLOCK.

The time incrementation scheme can be better illustrated by the two separate solvers in Fig. 5. The mechanical solver by FEM is based on the Newton–Raphson method to solve the nonlinear Eq. (1) upon finite element discretization. Therefore, UEL subroutine requires the calculation of CZM Jacobian to assemble the element stiffness matrix, and tractions at t_{n+1} to calculate the

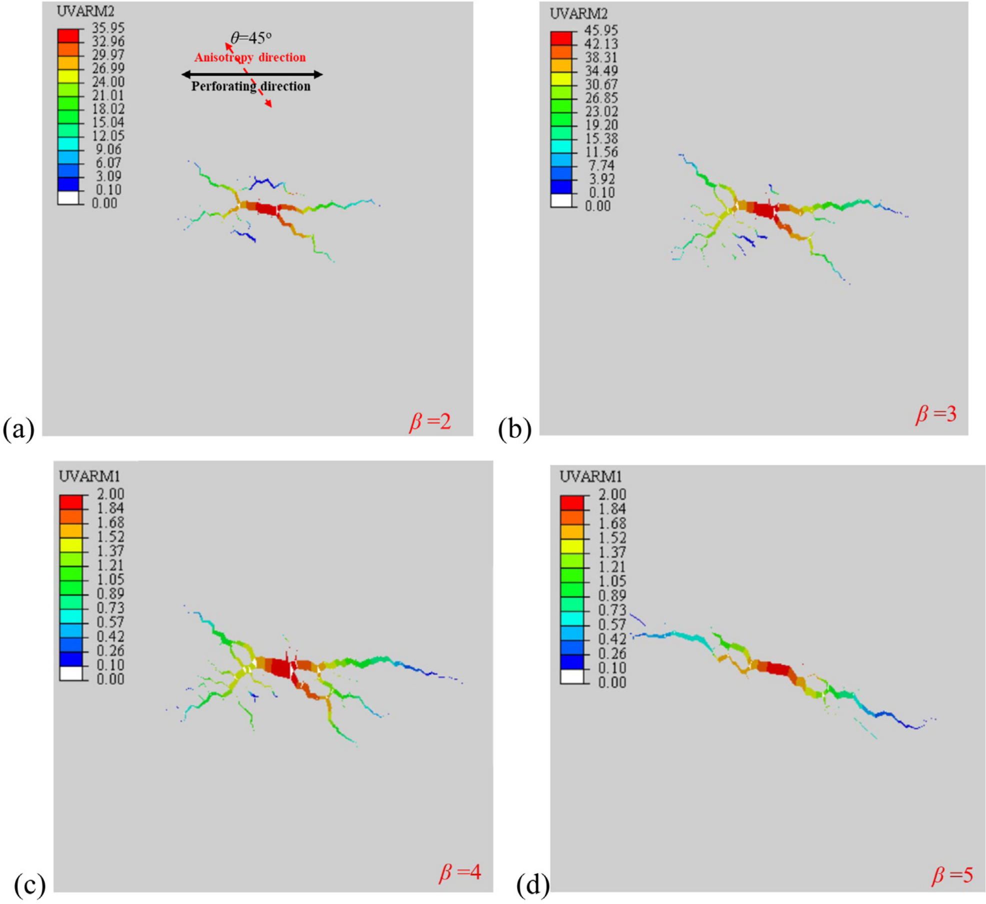

Fig. 12. Fracture morphologies due to fluid injection in the center (Fig. 9) with material anisotropy direction lying at $\theta = 45°$: (a) $\beta = 2$, (b) $\beta = 3$, (c) $\beta = 4$, (d) $\beta = 5$.

residual vector. As shown in Fig. 1, the fluid pressure is taken as applied force onto the cohesive elements, and thus incorporated into the UEL residual vector by replacing T_n by $T_n - p$. The related tangent, $\partial p/\partial \Delta_n$, is however not added to the UEL stiffness matrix; in other words, we are using a semi-consistent Jacobian for the Newton–Raphson iteration. Nevertheless, FEM convergence is rather fast and any numerical difficulties associated with crack nucleation can be resolved by the fictitious viscosity in Eqs. (7) and (8), and the related time steps are chosen by ABAQUS automatic incrementation algorithm as determined from the radius of convergence calculation for the Newton–Raphson iterations. On the other hand, the hydraulic solver takes cohesive element separations as inputs and update the pressure fields from the FD approach. The governing equation is parabolic and thus the time step has to be chosen according to fluid viscosity and element size as shown in Eq. (12). In other words, it is sometimes necessary to discretize $[t_n, t_{n+1}]$ into many time bins to ensure numerical stability.

3. Validation

In this section, our numerical framework is validated against the analytical KGD solution, which was first proposed by Khristianovic and Zhelton [35] and then improved by Geertsma and de Klerk [5]. It addresses the propagation of a single crack, due to the injection of an incompressible fluid under a constant rate, in an infinite, brittle elastic solid under uniform pressure as shown in Fig. 6(a). The crack half-length and the opening were derived as [36]:

$$L_{KGD}(t) = C_1 \left(\frac{E' q_0^3}{\mu} \right)^{\frac{1}{6}} t^{\frac{2}{3}} \tag{13}$$

$$w_{KGD}(t) = C_2 \left(\frac{\mu q_0^3}{E'} \right)^{\frac{1}{6}} t^{\frac{1}{3}} \tag{14}$$

where q_0 is the injection rate per unit height of the fracture, $E' = 2E/\left(1 - \nu^2\right)$ is the plane strain modulus of the rock with the Young's modulus E and Poisson's ratio ν, and C_1 and C_2 are numerical factors. Due to numerous assumptions in the KGD model such as a uniform flow rate along the fracture and no explicit dependence of the solution on the fracture toughness, our validation is focused on the parametric grouping and power exponents in Eqs. (13) and (14), rather than on the exact values of the pre-factors.

As shown in Fig. 6(b), the numerical example simulates the propagation of a straight and vertical crack driven by injecting fluid at a constant flow rate into an elastic, homogeneous rock. The simulation domain is of 10 m × 10 m with impermeable surrounding boundaries and fluid injection at the top element. Material and fluid properties are listed in Table 1. The mesh size is chosen based on the following considerations. When a cohesive constitutive law is introduced to smear out the stress singularity in the linear elastic fracture mechanics, the corresponding crack bridging zone is thus given by [30]

$$\text{bridging zone} \approx 0.2 \frac{E}{\sigma_{\max}} \delta_n, \tag{15}$$

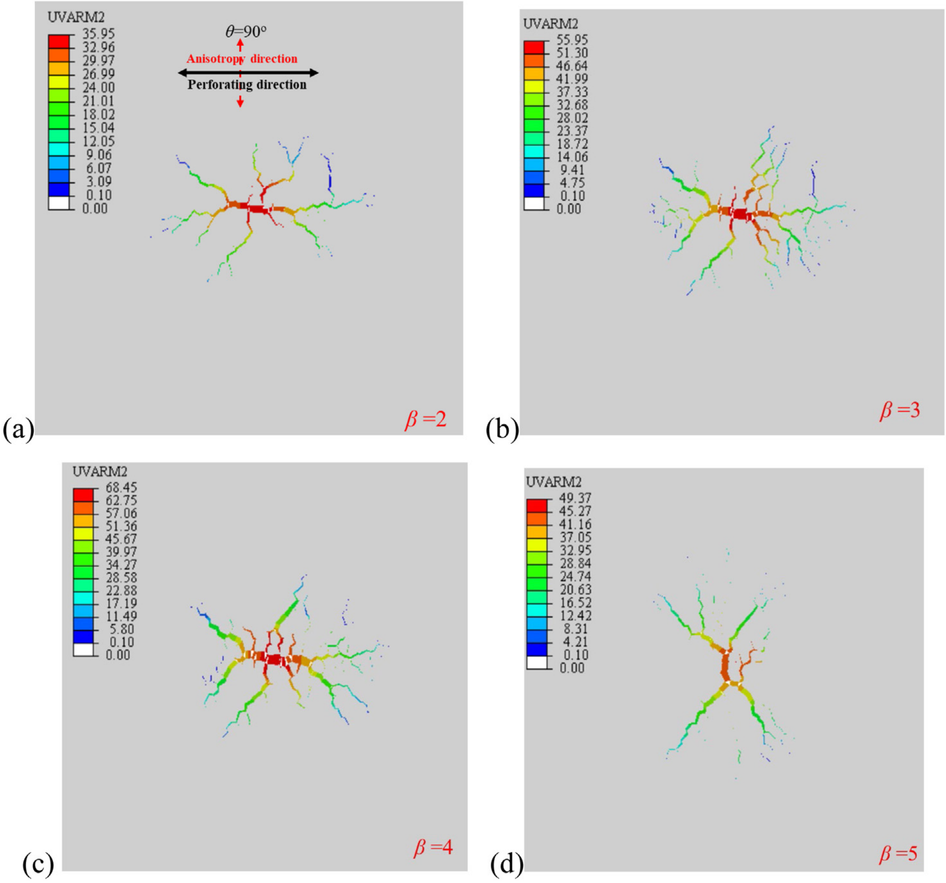

Fig. 13. Fracture morphologies due to fluid injection in the center (Fig. 9) with material anisotropy direction lying at $\theta = 90°$: (a) $\beta = 2$, (b) $\beta = 3$, (c) $\beta = 4$, (d) $\beta = 5$.

where the pre-factor of 0.2 is based on numerical simulations. The mesh size should be smaller than or comparable to this value, rather than δ_n (which is impossible to resolve in such simulations). In this case, this bridging zone size is orders of magnitude smaller than the crack size, thus corresponding to the crack nucleation problem. Without the use of fictitious viscosity, the finite element calculations will encounter difficulty in attaining numerical convergence.

A good agreement between the analytical solutions and the numerical simulation is found in Fig. 7, from which we fit $C_1 = 0.34$ from Fig. 7(a) and $C_2 = 3.3$ from Fig. 7(b). Numerical simulations calculate the fluid flow rate that is coupled with the deformation field in the rock. The obtained evolution of pressure gradient fields in Fig. 7(c) clearly defies the KGD assumption of a uniform pressure field. Fracture opening along fracture length is also shown in Fig. 7(d). Our choices of cohesive properties lead to a quite small bridging zone size so that they rather have a minimal effect on the fracture length. The fracture toughness may have a large effect on the fracture length, but the actual values of rocks do not differ noticeably from ~2.1 MPa $\sqrt{\text{m}}$ from Table 1 so that our simulations are of quintessential nature.

4. Anisotropic hydraulic fracture

Not all grain boundaries in geomaterials are weak surfaces, as some natural fracture and bedding planes are more prone to failure in shale reservoir [26,31,37]. As shown in Fig. 8(a), these planes are filled with minerals and not able to contribute to the reservoir storage or conductivity, but they bring serious crack branching and anisotropic fracture to rock materials. We also note the relative degree of opening and shear modes changes in various crack branches, as illustrated in Fig. 8(b).

To investigate the effect of rock anisotropy on fracture geometry, a hydraulic fracturing simulation with random grains is presented. The use of Voronoi tessellation generates random polygonal grains with controllable shape distributions, which guarantees that the macroscopic behavior of reservoirs is not biased by any spurious particle distributions [38]. As shown in Fig. 9, a polycrystalline model of 25 m × 25 m with confining pressures σ_H and σ_h is created to represent the reservoir rock. The hydraulic flow is injected into a fracture element in the center of the model, and the perforating direction (or initial fracture orientation) is also marked.

Previous works in [17,39,40] have focused on the role of elastic anisotropy on the growth direction of individual cracks. In contrast, our work here is motivated by the experimental observations in Fig. 8, and thus considers the fracture anisotropy. We note that there are two independent directions in our simulations, one being the element orientation as characterized by α in Fig. 9, and the other being the material anisotropy direction (or symmetry line) as shown later by θ in Figs. 11 and 12. We now assume the cohesive strength depends on $|\theta - \alpha|$ as a four-fold symmetry function,

$$\frac{\sigma_{\max}(\theta, \alpha)}{\sigma_{\max}(MIN)} = 1 + (\beta - 1)\sin|\theta - \alpha|, \tag{16}$$

where the parameter β determines the degree of anisotropy. The cohesive characteristic lengths are prorated similarly, as shown in Fig. 10 where $|\theta - \alpha| = \pi/2$.

Hydromechanical parameters used in our simulations are listed in Table 2, and representative results are given in Figs. 11 and 12,

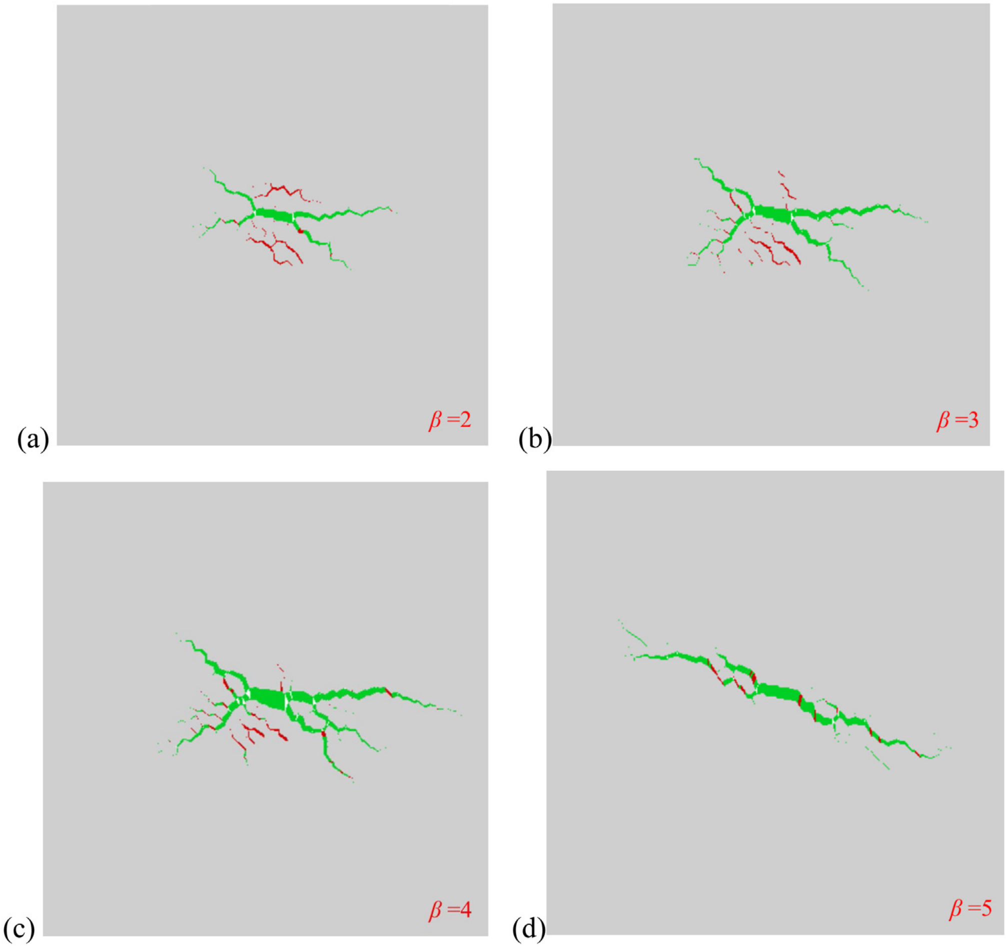

Fig. 14. Crack failure types, where green means tensile failure and red means shear failure with material anisotropy direction lying at $\theta = 45°$: (a) $\beta = 2$, (b) $\beta = 3$, (c) $\beta = 4$, (d) $\beta = 5$. (For interpretation of the references to color in this figure legend, the reader is referred to the web version of this article.)

whereas UVARM2 shows the fluid pressure. The crack is initially horizontal as forced by the element directions at the center of the model, but whether this central crack will deflect depends on θ and β. In Fig. 11, $\theta = 0°$ and thus Eq. (16) dictates that the horizontally lying elements are weak surfaces. Consequently, the crack morphology will tend to be horizontal, and more so at a higher value of β. The zig-zag nature arises from the graininess nature of the material.

In Fig. 12, the perforating direction and the strength anisotropy direction make an angle of $\theta = 45°$. While the weak surfaces are at 45° off the perforating direction, the final crack morphology approaches this inclined direction only for a high value of β as shown in Fig. 12(b). The transitional behavior of crack morphology and branching clearly depends on the particular choice in Eq. (16), but these results demonstrate the computational capability of our numerical approach and can be easily extended to realistic application problems.

In order to compare to experiments in Fig. 8(b), we plot the failure modes in Figs. 14 and 15, which correspond to the crack opening displacement results in Figs. 12 and 13, respectively. When the perforating direction is not parallel to the fracture energy anisotropy direction, we will see multiple secondary branches in predominately shear fracture mode. These findings are in good agreement with previous experiments in Fig. 8(b), suggesting the importance of the complex interplays amongst anisotropy, fracture morphology, and fracture model.

5. Summary

This study proposes a numerical approach to simulate hydraulic fracture propagation by a coupled FEM/FD formulation. The nonlinear FEM implementation of the cohesive interface model into ABAQUS UEL subroutine provides a user-friendly interface to incorporate more advanced hydromechanical constitutive laws. The FD solver for fluid flow provides the updated pressure field as inputs to the residual vector for the UEL. The nonlocal information needed for FD is obtained from the COMMON BLOCK technique, and the time incrementation can be treated separately for nonlinear FEM and FD procedures. Our numerical scheme has been successfully verified against the KGD analytical solution. Furthermore, our approach is capable of capturing complex fracture patterns and branching behavior. In this case, the geomaterial can be modeled as a polycrystal with Voronoi tessellation, and the grain boundaries can represent flaws for fracture propagation. Considering materials with fracture anisotropy, our simulation results found that, when the anisotropy direction is not in alignment with the perforating direction, a complex fracture morphology may appear during the fracking process. When the degree of fracture anisotropy increases, the fracture pattern eventually turns to the weakest direction. These simulation results are amenable to further experimental comparisons.

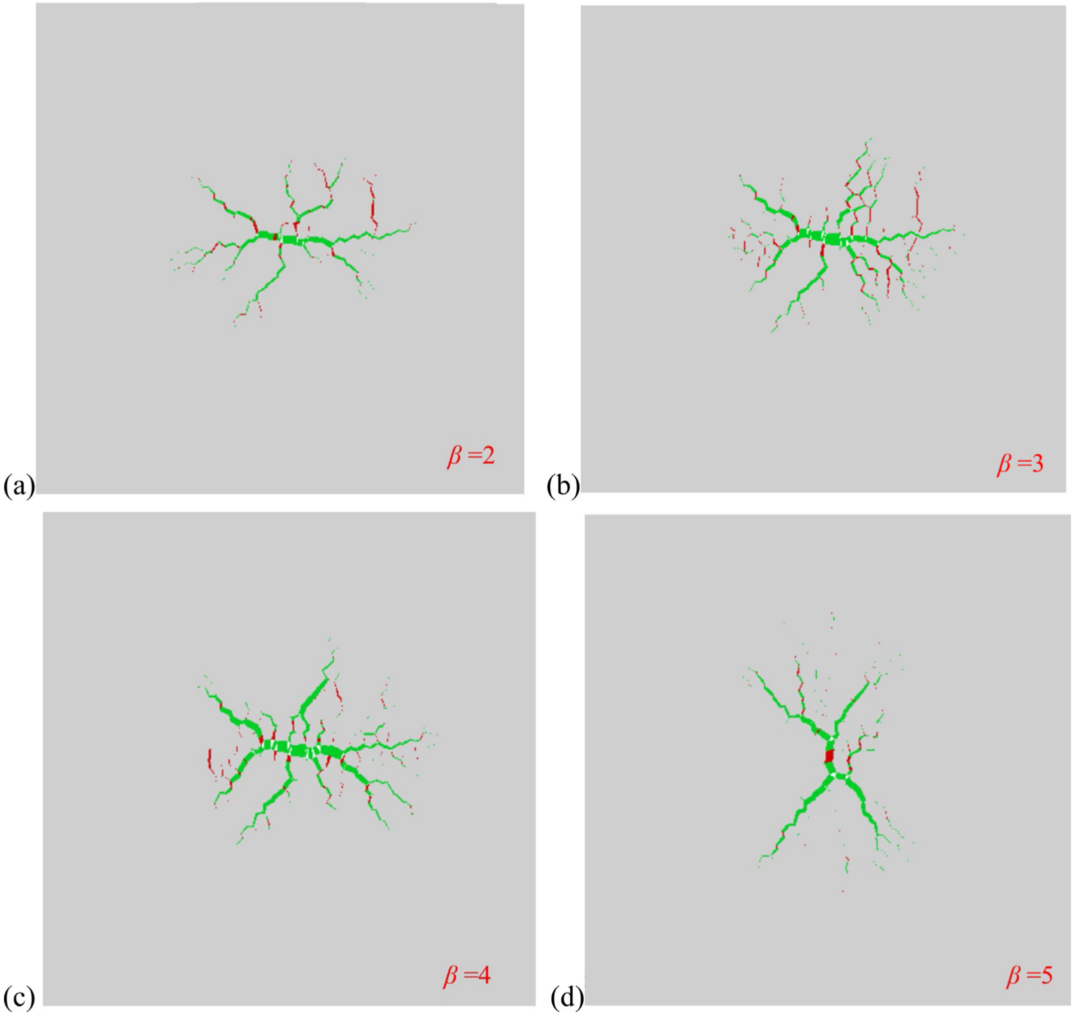

Fig. 15. Crack failure types, where green means tensile failure and red means shear failure with material anisotropy direction lying at $\theta = 90°$: (a) $\beta = 2$, (b) $\beta = 3$, (c) $\beta = 4$, (d) $\beta = 5$. (For interpretation of the references to color in this figure legend, the reader is referred to the web version of this article.)

Declaration of competing interest

The authors declare that they have no known competing financial interests or personal relationships that could have appeared to influence the work reported in this paper.

Data availability

Data contained in this paper are available upon request to the corresponding authors.

Acknowledgments

This work is funded by National Science and Technology Major Project of China (2017ZX05009005) for the work performed at China University of Petroleum, the China Scholarship Council for the one-year academic visit of XC to the University of Tennessee, and the US National Science Foundation DMR-1809640 for YFG.

References

[1] B. Cecampion, A. Bunger, X. Zhang, Numerical methods for hydraulic fracture propagation: A review of recent trends, J. Nat. Gas Sci. Eng. 49 (2018) 66–83.

[2] Y. Liu, D. Gao, Q. Li, Y. Wan, W. Duan, X. Zeng, M. Li, Y. Su, Y. Fan, S. Li, X. Lu, D. Zhou, W. Chen, Y. Fu, C. Jiang, S. Hou, L. Pan, X. Wei, Z. Hu, X. Duan, S. Gao, R. Shen, J. Chang, X. Li, Z. Liu, Y. Wei, Z. Zheng, Mechanical frontiers in shale-gas development, Adv. Mech. 49 (2019) 201901.

[3] J. Adachi, E. Siebrits, A. Peirce, J. Desroches, Computer simulation of hydraulic fractures, Int. J. Rock Mech. Min. Sci. 44 (2007) 739–757.

[4] R.P. Nordgren, Propagation of a vertical hydraulic fracture, Soc. Pet. Eng. J. 12 (1972) 306–314.

[5] J. Geertsma, F. De Klerk, A rapid method of predicting width and extent of hydraulically induced fractures, J. Pet. Tech. 21 (1969) 1571–1581.

[6] L. Vandamme, J.H. Curran, A three-dimensional hydraulic fracturing simulator, Internat. J. Numer. Methods Engrg. 28 (1989) 909–927.

[7] J.E. Olson, K. Wu, Sequential vs. simultaneous multizone fracturing in horizontal wells: insights from a non-planar, multifrac numerical model, in: SPE Hydraulic Fracturing Technology Conference, SPE-152602-MS, 2012.

[8] Z. Chen, M. Wang, Pore-scale modeling of hydromechanical coupled mechanics in hydrofracturing process, J. Geophys. Res.: Solid Earth 122 (2017) 3410–3429.

[9] S.A.G. Torres, J.D.M. Castaño, Simulation of the hydraulic fracture process in two dimensions using a discrete element method, Phys. Rev. E 75 (2007) 066109.

[10] X. Zhao, R.P. Young, Numerical modeling of seismicity induced by fluid injection in naturally fractured reservoirs, Geophysics 76 (2011) WC167–WC180.

[11] B.J. Carter, J. Desroches, A.R. Ingraffea, P.A. Wawrzynek, Simulating fully 3D hydraulic fracturing, Model. Geomech. 200 (2000) 525–557.

[12] M. Wangen, Finite element modeling of hydraulic fracturing on a reservoir scale in 2D, J. Pet. Sci. Eng. 77 (2011) 274–285.

[13] M. Wangen, Finite element modeling of hydraulic fracturing in 3D, Comput. Geosci. 17 (2013) 647–659.

[14] M.W. McClure, R.N. Horne, An investigation of stimulation mechanisms in enhanced geothermal systems, Int. J. Rock Mech. Min. Sci. 72 (2014) 242–260.

[15] H. Shimizu, S. Murata, T. Ishida, The distinct element analysis for hydraulic fracturing in hard rock considering fluid viscosity and particle size distribution, Int. J. Rock Mech. Min. Sci. 48 (2011) 712–727.

[16] T. Mohammadnejad, A.R. Khoei, An extended finite element method for hydraulic fracture propagation in deformable porous media with the cohesive crack model, Finite Elem. Anal. Des. 73 (2013) 77–95.

[17] Q.D. Zeng, J. Yao, J.F. Shao, Study of hydraulic fracturing in an anisotropic poroelastic medium via a hybrid EDFM-XFEM approach, Comput. Geotech. 105 (2019) 51–68.

[18] Y. Wei, L. Anand, On micro-cracking, inelastic dilatancy, and the brittle–ductile transition in compact rocks: A micro-mechanical study, Int. J. Solids Struct. 45 (2008) 2785–2798.

[19] J.H. Lee, Y.F. Gao, K.E. Johanns, G.M. Pharr, Cohesive interface simulations of indentation cracking as a fracture toughness measurement method for brittle materials, Acta Mater. 60 (2012) 5448–5467.

[20] X.P. Xu, A. Needleman, Numerical simulations of fast crack growth in brittle solids, J. Mech. Phys. Solids 42 (1994) 1397–1434.

[21] Z. Chen, A.P. Bunger, X. Zhang, R.G. Jeffrey, Cohesive zone finite element-based modeling of hydraulic fractures, Acta Mech. Solida Sin. 22 (2009) 443–452.

[22] Z. Chen, Finite element modelling of viscosity-dominated hydraulic fractures, J. Pet. Sci. Eng. 88–89 (2012) 136–144.

[23] J. Zou, W. Chen, J. Yuan, D. Yang, J. Yang, 3-D numerical simulation of hydraulic fracturing in a CBM reservoir, J. Nat. Gas Sci. Eng. 37 (2017) 386–396.

[24] ABAQUS Analysis User Manual (V6.12), V2017, Dassault, Providence, RI, USA, 2017.

[25] V.P. Nguyen, H. Lian, T. Rabczuk, S. Bordas, Modelling hydraulic fractures in porous media using flow cohesive interface elements, Eng. Geol. 225 (2017) 68–82.

[26] G.A. Waters, J.R. Heinze, R. Jackson, A.A. Ketter, J.L. Daniels, D. Bentley, Use of horizontal well image tools to optimize Barnett shale reservoir exploitation, in: SPE Annual Technical Conference and Exhibition, SPE-103202-MS, 2006.

[27] A. Needleman, Some issues in cohesive surface modeling, Procedia IUTAM 10 (2014) 221–246.

[28] B. Carrier, S. Granet, Numerical modeling of hydraulic fracture problem in permeable medium using cohesive zone model, Eng. Fract. Mech. 79 (2012) 312–328.

[29] Y. Yao, L. Liu, L.M. Keer, Pore pressure cohesive zone modeling of hydraulic fracture in quasi-brittle rocks, Mech. Mater. 83 (2015) 17–29.

[30] Y.F. Gao, A.F. Bower, A simple technique for avoiding convergence problems in finite element simulations of crack nucleation and growth on cohesive interfaces, Modelling Simul. Mater. Sci. Eng. 12 (2004) 453–463.

[31] T. Zhou, S. Zhang, Y. Feng, Y. Shuai, Y. Zhou, N. Li, Experimental study of permeability characteristics for the cemented natural fractures of the shale gas formation, J. Nat. Gas Sci. Eng. 29 (2016) 345–354.

[32] T. Guo, S. Zhang, Z. Qu, T. Zhou, Y. Xiao, J. Gao, Experimental study of hydraulic fracturing for shale by stimulated reservoir volume, Fuel 128 (2014) 373–380.

[33] M.S.H. Al-Gharbi, Dynamic Pore-Scale Modelling of Two-Phase Flow, University of London, 2004.

[34] C. Pu, Y.F. Gao, Y.L. Wang, T.L. Sham, Diffusion-coupled cohesive interface simulations of stress-corrosion intergranular cracking in polycrystalline materials, Acta Mater. 136 (2017) 21–31.

[35] S.A. Khristianovic, Y.P. Zhelton, Formation of vertical fractures by means of highly viscous liquid, in: World Petroleum Congress Proceedings, 1955, pp. 579–586.

[36] P. Valko, M.J. Economides, Hydraulic Fracture Mechanics, Wiley, 1995.

[37] J.F.W. Gale, J. Holder, Natural Fractures in Some US Shales and Their Importance for Gas Production, in: Petroleum Geology Conference Series, Vol. 7, Geological Society of London, 2010, pp. 1131–1140.

[38] E. Ghazvinian, M.S. Diederichs, R. Quey, 3D random Voronoi grain-based models for simulation of brittle rock damage and fabric-guided micro-fracturing, J. Rock Mech. Geotech. Eng. 6 (2014) 506–521.

[39] J.P. Zou, W.Z. Chen, Y.Y. Jiao, Numerical simulation of hydraulic fracture initialization and deflection in anisotropic unconventional gas reservoirs using XFEM, J. Nat. Gas Sci. Eng. 55 (2018) 466–475.

[40] M.R. Chandler, P.G. Meredith, N. Brantut, B.R. Crawford, Fracture toughness anisotropy in shale, J. Geophys. Res. Solid Earth 121 (2016) 1706–1729.